RSC Advances

PAPER

View Article Online
View Journal | View Issue

Cite this: *RSC Adv.*, 2018, **8**, 12459

Heterostructured Bi_2S_3@NH_2-MIL-125(Ti) nanocomposite as a bifunctional photocatalyst for Cr(VI) reduction and rhodamine B degradation under visible light†

Minghua Wang,[ab] Longyu Yang,[b] Jinyun Yuan,[b] Linghao He,[ab] Yingpan Song,[b] Hongzhong Zhang,[a] Zhihong Zhang *[ab] and Shaoming Fang*[ab]

Received 29th January 2018
Accepted 21st March 2018

DOI: 10.1039/c8ra00882e

rsc.li/rsc-advances

A series of bismuth sulfide (Bi_2S_3) nanorods and amine-functionalized Ti-based metal–organic framework heterojunctions [denoted by Bi_2S_3@NH_2-MIL-125(Ti)] were constructed and explored as bifunctional photocatalysts for Cr(VI) reduction and rhodamine B (RhB) degradation under visible light illumination. Compared with the individual NH_2-MIL-125(Ti) and Bi_2S_3, the as-synthesized Bi_2S_3@NH_2-MIL-125(Ti) photocatalyst exhibited an enhanced photocatalytic activity toward Cr(VI) and RhB owning to the synergetic effect between Bi_2S_3 and NH_2-MIL-125(Ti). Moreover, the Bi_2S_3@NH_2-MIL-125(Ti) heterojunctions showed increased Cr(VI) removal efficiency by adding RhB in the system. The photocatalytic mechanism was proposed based on the analysis of different scavenger for active species and electron spin resonance spectrometry. The introduction of Bi_2S_3 into NH_2-MIL-125(Ti) can extend the light adsorption and improve the transfer and separation of photogenerated charge carriers through the Bi_2S_3@NH_2-MIL-125(Ti) heterojunction with unique band gap structure. The synthesized Bi_2S_3@NH_2-MIL-125(Ti) photocatalyst also exhibited good reusability and stability.

Introduction

A variety of aromatic organic pollutants, including dyes, phenol, naphthalene, and trichloroethylene, have been found at high concentrations in water containing inorganic pollutants such as Cr(VI), Pb(II), and Hg(II). Due to their acute toxicity and bioaccumulation, the removal of these contaminants from wastewater is particularly significant. For the past few years, photocatalytic technology has emerged as a highly effective, low-cost, and eco-friendly treatment for hazardous pollutants by utilizing solar energy.[1] According to other studies, heavy metal ion reduction and organic pollutant degradation can simultaneously occur in the photocatalytic process.[2] For instance, the synergistic effect between the removal of Cr(VI) and degradation of organic pollutants is revealed by multiple utilization of TiO_2 nanorods/g-C_3N_4 for photocatalytic activity.[3] Nevertheless, the highly efficient and simultaneous photocatalytic removal of the co-existing pollutants remains a challenged due to the limited utilization of sunlight, rapid recombination of photogenerated electron–hole pairs, and relatively low specific surface area.

Recently, as a new class of porous materials with an extended 3D network, metal–organic frameworks (MOFs), which are composed of metal containing nodes and organic linkers, exhibit given chemical stability and structural tenability.[4,5] As such, MOFs and their derivatives showed potential applications in gas storage and separation,[6–8] catalysis,[9,10] and biomedical applications.[11–13] Additionally, owing to the high surface area, structural organization and adjustiability of MOFs, scientists have focused on their photocatalytic performances, such as in photocatalytic decontamination of organic pollutants, heavy metal, and photocatalytic water splitting.[14–17] For instance, the PANI/FeUiO-66 nanohybrids exhibited high photocatalytic performances toward the oxidation of various alcohol substrates.[18] As a photo-response and highly porous material, NH_2-MIL-125(Ti) has shown great potential in hydrogen production,[19] CO_2 reduction,[20] the removal of organic pollutants[21] and Cr(VI).[22] As reported, the NH_2-MIL-125(Ti) framework only exhibited single catalytic performance toward the specific pollution. It demonstrated the combination of NH_2-MIL-125(Ti) and other photocatalytic active inorganic compounds can improve its photocatalytic ability. For example, BiOBr/NH_2-MIL-125(Ti) composite possesses an enhanced photocatalytic performance, by which 80% of RhB was degraded under visible light irradiation within 100 min. The RhB degradation rate for

[a]Henan Collaborative Innovation Center of Environmental Pollution Control and Ecological Restoration, P. R. China

[b]Henan Provincial Key Laboratory of Surface & Interface Science, Zhengzhou University of Light Industry, Zhengzhou, 450001, P. R. China. E-mail: mainzhh@163.com; mingfang@zzuli.edu.cn

† Electronic supplementary information (ESI) available. See DOI: 10.1039/c8ra00882e

BiOBr/NH_2-MIL-125(Ti) was 3.12-fold that of pure BiOBr and 5.64-fold that of pure NH_2-MIL-125(Ti).[23] However, it remained a huge challenge to explore the bifunctionally catalytic activity of NH_2-MIL-125(Ti) toward multi-pollutions in the environmental system.

As an n-type semiconductor, bismuth sulfide (Bi_2S_3) has a bulk narrow direct band gap (~1.3 eV) with an extended visible light absorption.[24] Nanostructured Bi_2S_3 materials have been used as functional broad-spectral photosensitizer.[25] Gao *et al.* reported that the prepared mesoporous hetero-structured $BiVO_4/Bi_2S_3$ hollow discoid exhibited improved photoelectrochemical current response and efficient Cr(VI) removal under visible-light illumination.[26] The $Bi_2S_3/Bi_2O_2CO_3$ n–n-type heterojunction displayed good photocatalytic activity for degrading RhB under sunlight irradiation.[27] Compared with pure MOFs, catalysts based on the heterostructure combination of MOFs with metal oxide/sulfides/metals showed great advantages due to their synergetic effect.[28–30] However, few studies were conducted on the preparation of the Bi_2S_3 and MOF heterojunction photocatalysts for the removal of pollutants. To the best of our knowledge, no report has been published on the simultaneous removal of Cr(VI) and RhB by using NH_2-MIL-125(Ti)-based photocatalyst.

Based on above analysis, we designed and prepared a series of heterostructured Bi_2S_3@NH_2-MIL-125(Ti) nanocomposites *via* solvothermal method, which exhibit the highly enhanced photocatalytic activity for the simultaneous removal of Cr(VI) and RhB. As compared to the routine photocatalysts, the as-synthesized Bi_2S_3@NH_2-MIL-125(Ti) possesses substantial three advantages, including (i) improved visible light harvesting owing to Bi_2S_3 and $-NH_2$ containing in the ligands of MOF; (ii) effective photoinduced charge carriers transfer and separation in Bi_2S_3@NH_2-MIL-125(Ti) heterojunction with matched band gap structure; and (iii) synergetic effect between Bi_2S_3 and NH_2-MIL-125(Ti) for construction of bifunctional photocatalyst toward Cr(VI) and organic pollutants. It demonstrated that the as-prepared Bi_2S_3@NH_2-MIL-125(Ti) photocatalyst exhibited an enhanced visible light photocatalytic activity for Cr(VI) reduction and RhB degradation as compared to pure NH_2-MIL-125(Ti) and pure Bi_2S_3.

Experiment section

Materials and reagents

Tetra-*n*-butyl titanate ($Ti(OC_4H_9)_4$) and 2-aminoterephthalic acid ($H_2BDC\text{-}NH_2$, $C_8H_7NO_4$) were purchased from Aladdin Chemistry Co., Ltd. (Shanghai, China). *N*, *N*-Dimethylformamide (DMF), CH_3OH, ethylene glycol (EG), $K_2Cr_2O_7$, and PVP (MW 40000) were obtained from Kemi European Chemical Reagent Co., Ltd. (Tianjin, China). All reagents were of analytical grade, whereas all solutions were prepared with Milli-Q ultrapure water (≥18.2 MΩ cm).

Preparation of Bi_2S_3@NH_2-MIL-125(Ti) nanocomposites

Bi_2S_3 nanorods was synthesized by according to the previous report[31] and NH_2-MIL-125(Ti) was prepared using $H_2BDC\text{-}NH_2$ as organic linker *via* solvothermal method,[10,32] as described in detail in the ESI (see S1†).

To prepare Bi_2S_3@NH_2-MIL-125(Ti) nanocomposites, a certain amount of Bi_2S_3 (10, 50, and 100 mg) were added into beakers. Then, DMF (18 mL), methanol (2 mL), and PVP (0.5 g) were added into the beakers with stirring for 30 min under room temperature. Subsequently, 1.1 g 2-aminoterephthalic acid and 1.2 mL of tetrabutyl titanate were added into the beakers with stirring for 5 min. The resultant solution was poured into a Teflon-lined stainless-steel autoclave at 150 °C for 48 h. After reaction, the solid was centrifuged and washed repeatedly with DMF and methanol for several times and dried at 60 °C. The resultant Bi_2S_3@NH_2-MIL-125(Ti) nanocomposites with the amount of 10, 50, and 100 mg of Bi_2S_3 were denoted as Bi_2S_3@NM-10, Bi_2S_3@NM-50, and Bi_2S_3@NM-100, respectively.

Characterizations

X-ray diffraction (XRD) measurements were performed on a Rigaku D/Max-2500 X-ray diffractometer using Cu Kα radiation. The chemical structure and component of all sample were analyzed by Fourier transform infrared spectroscopy (FT-IR) (Bruker TENSOR27, Germany) and X-ray photoelectron spectroscopy (XPS) (Thermo Fisher ESCALAB 250Xi photoelectron spectrometer), respectively. Field emission scanning electron microscopy (FE-SEM) was conducted using a JSM-6490LV scanning electron microscope. Transmission electron microscopy (TEM) measurements were performed using a JEOL JSM-6490L V system. The UV-Visible photocatalytic apparatus used in this work is Japan model Hitachi U-3900H UV-Visible Spectrometer. The N_2 adsorption–desorption isotherms were conducted using a Micromeritics 3Flex surface area and pore size analyzer with a liquid nitrogen at the temperature of 77 K. The specific surface area was calculated by the Brunauer–Emmett–Teller (BET) method. Photoluminescence (PL) spectra were recorded on a Hitachi F-7000 fluorescence spectrophotometer.

Photocatalytic activity

$K_2Cr_2O_7$ and RhB were dissolved into deionized water to prepare Cr(VI) and RhB solution. The solution concentrations of Cr(VI) and RhB were 10 and 20 mg L^{-1}, respectively. A 300 W Xe lamp (PLS/SXE 300C, Beijing Perfectlight Co., Ltd.) equipped with a UV cutoff filter (λ > 420 nm) was used as the visible light source. The photocatalysts were added into the Cr(VI) and RhB solutions with continuous stirring for 30 min in the dark to achieve an adsorption–desorption equilibrium before irradiation. Afterward, the solution was irradiated under visible light with magnetic stirring. For photocatalytic analysis, 3 mL of suspensions at each given time interval were filtered with 0.45 μm filtration membrane. The concentrations of Cr(VI) were determined using colorimetry with the diphenylcarbazide as a color agent at 544 nm,[22] whereas those of RhB were determined by measuring the absorbance at 554 nm with UV-Vis spectrophotometer. For the recycle experiments of Cr(VI) reduction and RhB degradation, the used catalyst was collected by filtration, washed with deionized water and ethanol, and dried in a vacuum oven at 60 °C for the next run.

Different scavengers, including ethylene diamine tetraacetic acid (EDTA), isopropyl alcohol (IPA), benzoquinone (BQ), and $K_2S_2O_8$ were used to trap hole (h^+), hydroxyl radical ($^{\bullet}OH$), superoxide anion radical ($O_2^{\bullet-}$), and electron (e^-), respectively. The radical species were detected by electron spin resonance (ESR) spectrometry on a JES-FA spectrometer under visible light ($\lambda > 420$ nm). The 5,5-dimethyl-1-pyrroline *N*-oxide (DMPO) was selected as the spin-trapping agent in ESR spectrometry.

Electrochemical and photoelectrochemical analysis

The Mott–Schottky plots and photocurrent measurements were carried out on a CHI660D electrochemical analyzer in a traditional three electrode system, including a platinum as counter electrode, an indium-doped thin oxide (ITO) glass (1.5 × 3.0 cm) electrode as working electrode and an Ag/AgCl as reference electrode. The catalyst was dispersed and ultrasonicated in ethanol to form a homogeneous solution (8 mg mL^{-1}). Then, 40 μL of the solution was dropped onto the ITO glass and dried in a vacuum oven at 60 °C. The Mott–Schottky plots were obtained in 0.5 M Na_2SO_4 solution in dark. Amperometric *i–t* curves were obtained at an applied potential of 0.3 V *vs.* Ag/AgCl in 0.5 M Na_2SO_4 under visible light irradiation ($\lambda > 420$ nm).

Results and discussion

Chemical and crystal structure of as-prepared samples

The XRD patterns and FT-IR spectra of the as-prepared samples are displayed in Fig. 1a and b, respectively. The XRD pattern of NH_2-MIL-125(Ti) in Fig. 1a showed well-defined diffraction peaks (2θ) of 6.8°, 9.7°, 11.6°, 15.2°, and 19.5°, which agreed with those of the simulated XRD pattern.[32] The XRD pattern of Bi_2S_3 displayed typical 2θ at 15.8°, 17.6°, 22.4°, 23.7°, 24.9°, 25.2°, 27.4°, 28.7°, 31.7°, 32.9°, 34.0°, 35.7°, 39.9°, 45.6°, 46.5°, 48.3°, and 52.6°, which are indexed as the diffractions of (020), (120), (220), (101), (130), (310), (021), (211), (221), (301), (311), (240), (141), (002), (431), (060), and (351) crystalline planes of Bi_2S_3 orthorhombic phase (JCPDS card no. 17-0320).[33] The XRD patterns of the Bi_2S_3@NM samples exhibited the features of both Bi_2S_3 and NH_2-MIL-125(Ti), in which the feature of the former became increasingly evident with its increasing amount in the nanocomposites. For Bi_2S_3@NM-100, 2θ were found at 24.9°, 27.4°, 28.7°, and 31.7°, which corresponded to the (130), (021), (211), and (221) crystal planes of Bi_2S_3, respectively. The XRD diffraction peaks confirmed the successful synthesis of Bi_2S_3@NH_2-MIL-125(Ti) nanocomposites.

The strong and wide absorption band at approximately 3443 cm^{-1} in Fig. 1b was attributed to the primary amines ($-NH_2$) of the organic linker and the stretching vibration of the O–H groups of the adsorbed water. For Bi_2S_3 nanorods, the absorption peaks at 1630 cm^{-1} was ascribed to the C=O stretching vibration of carbamide. For NH_2-MIL-125(Ti) and Bi_2S_3@NM nanocomposites, the absorption bands at around 1559 and 1478 cm^{-1} were assigned to the ν (C=C) skeletal vibration of benzene ring contained in NH_2-MIL-125(Ti), whereas those at 1293 and 796 cm^{-1} were attributed to the C–H in-plane and out-of-plane bending vibrations, respectively. These results further confirmed the existence of NH_2-MIL-125(Ti) in the nanocomposite.

To identify the chemical composition and the chemical states of various as-prepared nanocomposites, XPS survey spectra were collected within the binding energy of 1 eV to 1200 eV (Fig. S1†). For NH_2-MIL-125(Ti), the Ti 2p signal was ascribed to the metal coordination center, whereas the C 1s, N 1s, and O 1s signals were caused by the organic ligands that link coordination centers. In addition to the signals of Bi 4p, Bi 4d, Bi 4f, S 2p, and S 2s, the C 1s signal was also observed in the XPS survey scan of Bi_2S_3, indicating the existence of the C element of the EG residue during fabrication. In the XPS survey spectra of Bi_2S_3@NM samples, the occurrence of C 1s, N 1s, O 1s, Ti 2p, Bi 4f, and S 2p suggested the presence of composites of Bi_2S_3 and NH_2-MIL-125(Ti). The atomic percentages of Bi 4f and S 2p increased from 0.04 to 0.19% and 0.18 to 1.98%, respectively, with the increasing Bi_2S_3 amounts contained in the nanocomposites (Table S1†).

The high-resolution XPS spectra of these samples are shown in Fig. 2 and S2–S4.† For NH_2-MIL-125(Ti) (Fig. S2a†), the

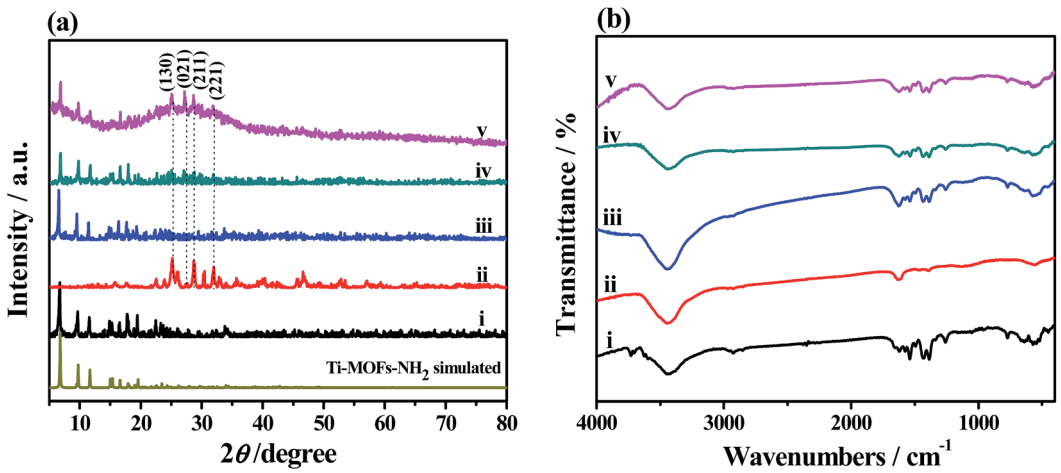

Fig. 1 (a) XRD patterns and (b) FT-IR spectra of (i) NH_2-MIL-125(Ti), (ii) Bi_2S_3, (iii) Bi_2S_3@NM-10, (iv) Bi_2S_3@NM-50, and (v) Bi_2S_3@NM-100 nanocomposites.

binding energies of Ti $2p_{3/2}$ and Ti $2p_{1/2}$ located at 458.7 and 464.5 eV, respectively, indicating titanium bounded to oxygen remains in oxidation state IV for the titanium-oxo cluster.[22] The C 1s spectrum of NH_2-MIL-125(Ti) (Fig. S2b†) showed four peaks at 284.6, 285.7, 287.4, and 288.7 eV, which were associated with the functional groups of C=C/C–H, C–N, C=O/N–C=O, and COO–, respectively. These functional groups were included in the ligands of NH_2-MIL-125(Ti) and the residual DMF in the framework. The N 1s spectrum can be fitted into three peaks at 399.3, 400.4, and 402.9 eV (Fig. S2c†), which were contributed to C–N/N–H, N–C=O, and $-N^+-$, respectively.[34] For the deconvoluted XPS spectrum of the O 1s (Fig. S2d†), two peaks were observed at 529.8 and 531.6 eV, which were derived from Ti–O and –OH groups,[21] respectively. As for Bi_2S_3 nanorods, the Bi $4f_{5/2}$ and Bi $4f_{7/2}$ at 157.5 and 162.8 eV with spin–orbit splitting of 5.3 eV were obtained in the high resolution spectrum of Bi 4f and corresponded to Bi^{3+} of the Bi_2S_3 nanoparticles (Fig. S3a†). The peaks at 160.2 and 161.4 eV can be ascribed to S $2p_{3/2}$ and S $2p_{1/2}$, respectively. The peak centered at around 224.6 eV can be attributed to S 2s of Bi_2S_3 (ref. 35) (Fig. S3b†). The signals of Ti 2p, Bi 4f, C 1s, N 1s, and O 1s of the series of Bi_2S_3@NM samples (Fig. 2 and S4†) were found to be consistent with those of the individual NH_2-MIL-125(Ti) and Bi_2S_3, suggesting the coexistence of the two components in the nanocomposites.

Surface morphologies of as-prepared samples

Fig. S5 and S6† display the FE-SEM and TEM images of NH_2-MIL-125(Ti) and Bi_2S_3, respectively. The NH_2-MIL-125(Ti) elucidated truncated bipyramids and octahedron structures with smooth surfaces. Bi_2S_3 exhibited the well-dispersed nanorods shape with a diameter of 20 to 40 nm and a length of 50 to 200 nm. The TEM and high-resolution TEM (HR-TEM) images of Bi_2S_3 illustrated the well-resolved lattice fringes with *d*-spacing of 0.504 nm, corresponding to orthorhombic (120) lattice plane of Bi_2S_3. The selected area electron diffraction (SAED) pattern (inset in Fig. S6d†) indicated the well-defined crystalline of Bi_2S_3. Fig. 3 shows the FE-SEM, TEM, and HR-TEM images of Bi_2S_3@NM nanocomposites. These images suggested that the size and distribution of the Bi_2S_3@NM nanocomposites become small and uniform with the increasing amounts of Bi_2S_3. The lattice spacing at 0.329, 0.188, and

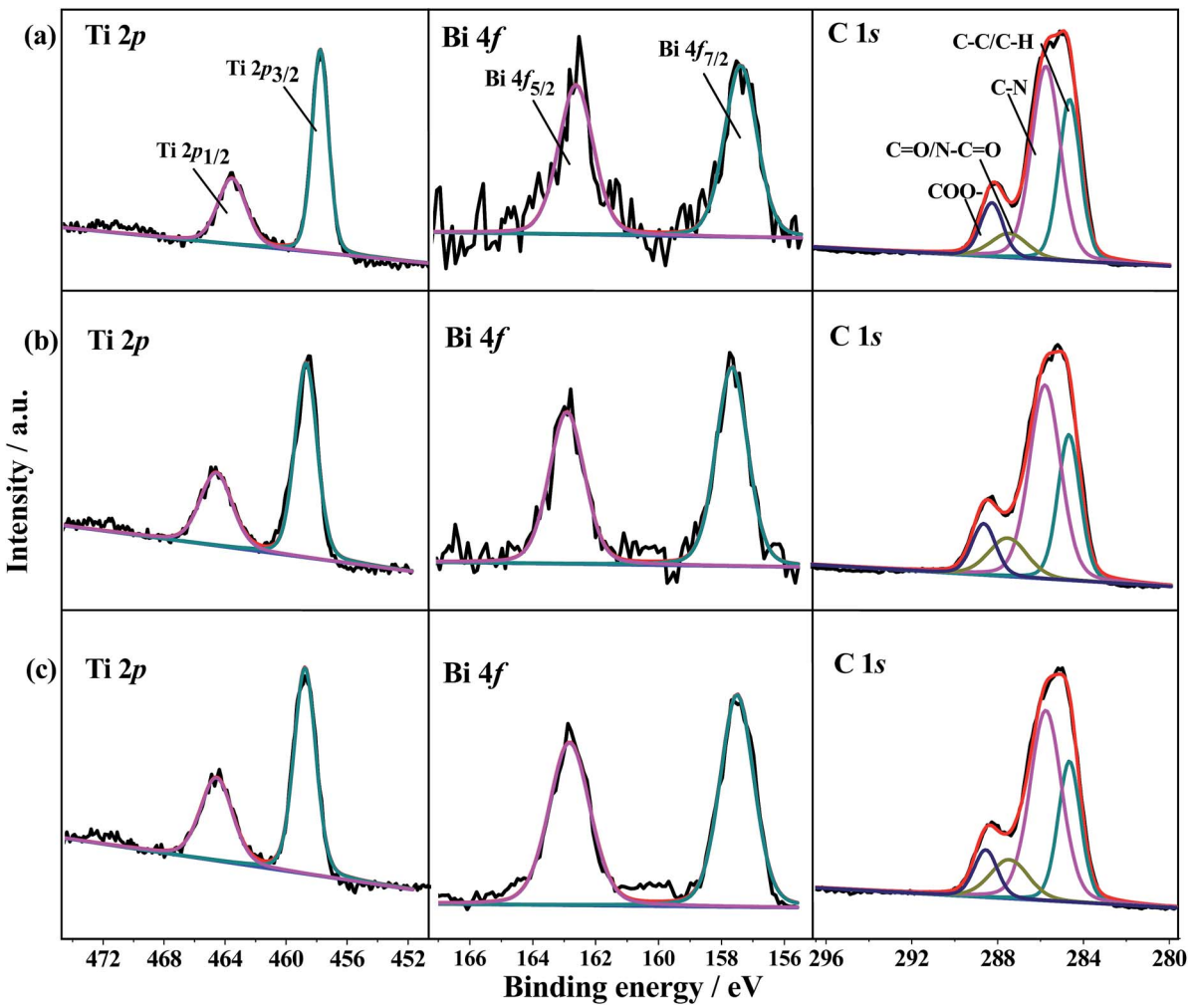

Fig. 2 Ti 2p, Bi 4f, and C 1s high resolution XPS spectra of (a) Bi_2S_3@NM-10, (b) Bi_2S_3@NM-50, and (c) Bi_2S_3@NM-100 nanocomposites.

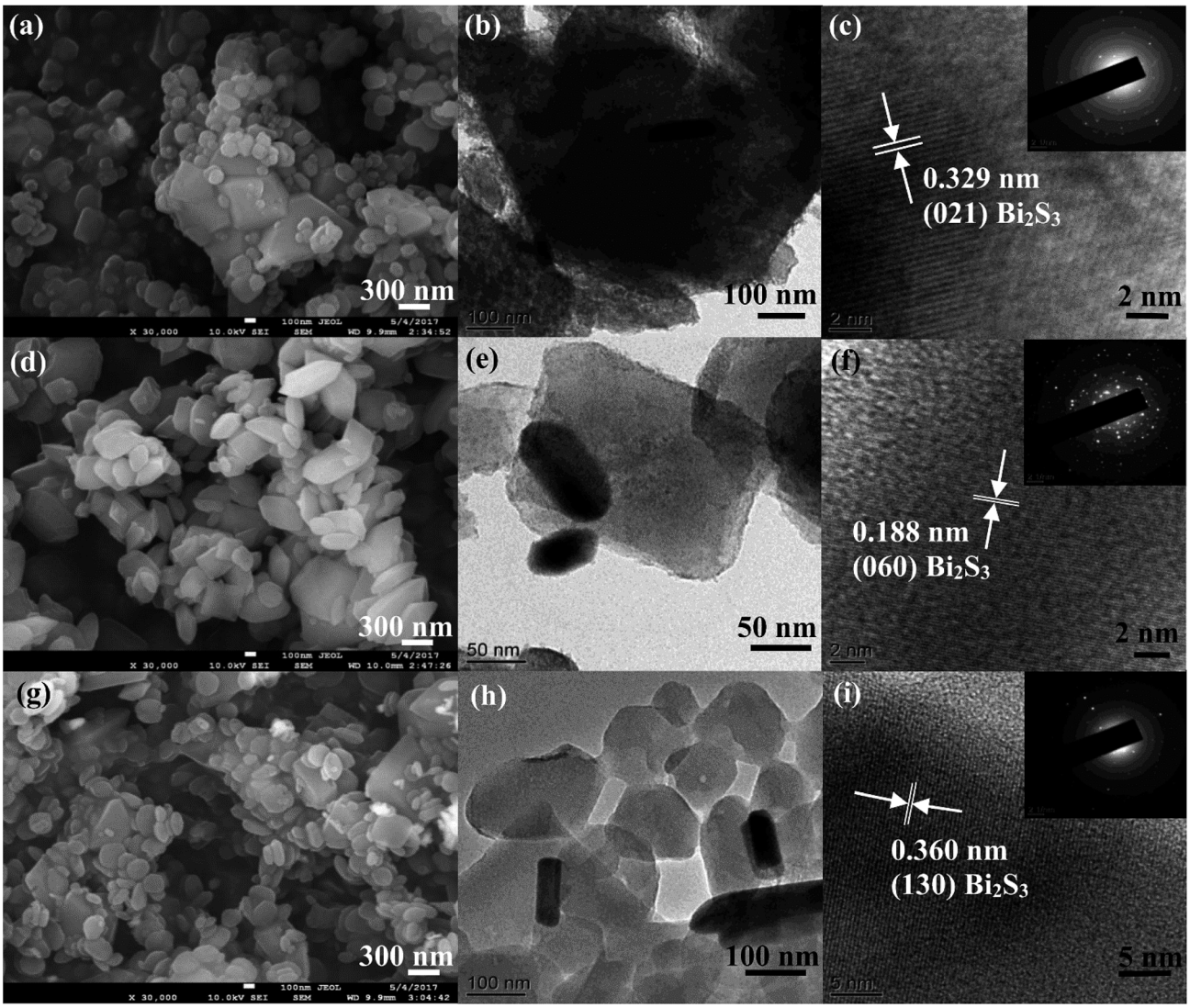

Fig. 3 FE-SEM, TEM and HR-TEM images of (a–c) Bi_2S_3@NM-10, (d–f) Bi_2S_3@NM-50, and (g–i) Bi_2S_3@NM-100 nanocomposites, respectively. The insets in (c), (f), and (i) are the corresponding SAED patterns.

0.360 nm were observed in the HR-TEM images of Bi_2S_3@NM nanocomposites, which are assigned to the (021), (060), and (130) planes of Bi_2S_3, respectively. All these results signified that the heterojunction of NH_2-MIL-125(Ti) and Bi_2S_3 was formed in the nanocomposites.

N_2 adsorption–desorption measurements shown in Fig. S7† indicated that the NH_2-MIL-125(Ti) still maintained the porous structure after recombining with Bi_2S_3. The specific surface areas were calculated as 485.7, 560.9, and 416.7 $m^2\ g^{-1}$ for Bi_2S_3@NM-10, Bi_2S_3@NM-50, and Bi_2S_3@NM-100 nanocomposites, respectively. The relatively high specific surface area of Bi_2S_3@NM nanocomposites was favorable to the adsorption of pollutants.

Optical and electrochemical properties

The optical absorption properties of NH_2-MIL-125(Ti), Bi_2S_3 and Bi_2S_3@NM nanocomposites were determined by UV-Vis DRS (Fig. 4a). The absorption edge of NH_2-MIL-125(Ti) was at ~500 nm, whereas the absorption onset of Bi_2S_3 was extended at ~1000 nm. The Bi_2S_3@NM nanocomposites exhibited better absorption than the pure NH_2-MIL-125(Ti) under the UV-Vis region, especially under visible light. Accordingly, the plot of $(\alpha h\nu)^2$ *versus* photo energy ($h\nu$) can be fitted into a linear pattern[36] (Fig. 4b). The band gaps of Bi_2S_3, NH_2-MIL-125(Ti), and Bi_2S_3@NM-10, Bi_2S_3@NM-50, and Bi_2S_3@NM-100 were calculated as 1.32, 2.68, 2.66, 2.64, and 2.59 eV, respectively. These results suggested that the introduction of Bi_2S_3 in favor of visible light absorption and thus facilitated the full utilization of solar energy.

PL spectra and photocurrent measurements were used to probe the recombination of photogenerated electrons and holes and charge carrier mobility of the photocatalysts. The PL intensities of all samples were normalized for comparison.[37] Fig. 5a shows that the NH_2-MIL-125(Ti) exhibited the highest PL intensity and thus possessed the highest recombination rate of

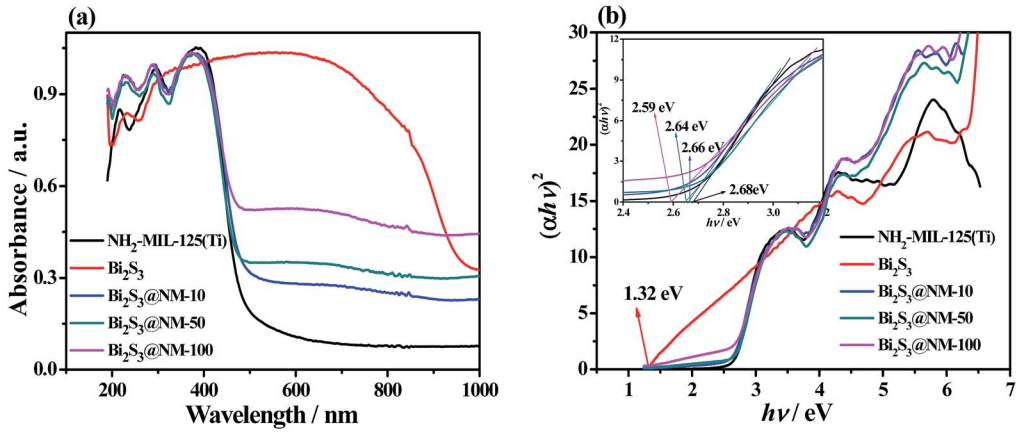

Fig. 4 (a) UV-Vis DRS and (b) the plots of $(\alpha h\nu)^2$ *versus* energy ($h\nu$) of the NH_2-MIL-125(Ti), Bi_2S_3, Bi_2S_3@NM-10, Bi_2S_3@NM-50, and Bi_2S_3@NM-100 (the inset: zoomed-in plots of the samples).

photo-induced electrons and holes. On the contrary, Bi_2S_3 exhibited the lowest PL intensity and thus possessed the lowest recombination efficiency of photogenerated charge carrier. The PL intensities of Bi_2S_3@NM nanocomposites were weaker than that of the pristine NH_2-MIL-125(Ti), which confirmed that the addition of Bi_2S_3 can effectively improve the seperation of photogenerated carriers. Photocurrent responses in Fig. 5b were measured under visible light in 0.5 M Na_2SO_4 aqueous solution. Among the photocatalysts, the photocurrent density of NH_2-MIL-125(Ti) was the lowest, whereas that of Bi_2S_3 was the highest. The photocurrent responses of the Bi_2S_3@NM increased with the increasing dosages of Bi_2S_3 in the nanocomposites. These results demonstrate that the separation and transfer of photogenerated carriers were improved *via* the introduction of Bi_2S_3.

Photocatalytic Cr(VI) reduction

Photocatalytic activities of different catalysts were evaluated through the reduction of Cr(VI). Fig. S8a–f† and 6a show UV-Vis absorption spectra and Cr(VI) reduction using NH_2-MIL-125(Ti), Bi_2S_3, and various Bi_2S_3@NM nanocomposites at pH of 7.0. Approximately 18% of Cr(VI) was reduced by the pure NH_2-MIL-125(Ti) and 48% by the pure Bi_2S_3 after illuminating for 120 min. The Bi_2S_3@NM samples exhibited higher photocatalytic activity than individual NH_2-MIL-125(Ti) and Bi_2S_3. Among the as-prepared nanocomposites, Bi_2S_3@NM-100 displayed the highest activity with 77% Cr(VI) removal under visible light for 120 min. As shown in Fig. 6b, the photocatalytic reactions followed the pseudo-first order reaction kinetic equation. The reaction rate was calculated by the apparent reaction rate constant (k) from the degradation curves of $-\ln(C/C_0)$ *versus* the irradiation time. Fig. S8g† confirms the k values of different samples, suggesting that the reaction rates of various samples were in the following order: NH_2-MIL-125(Ti) < Bi_2S_3 < Bi_2S_3@NM-10 < Bi_2S_3@NM-50 < Bi_2S_3@NM-100. The k value of Bi_2S_3@NM-100 (0.01134 min^{-1}) is 8.86-fold that of the NH_2-MIL-125(Ti) (0.00128 min^{-1}), and 3.57-fold that of the Bi_2S_3 (0.00318 min^{-1}), indicating that the photocatalytic Cr(VI) reduction was promoted by combining the two components. Therefore, the Bi_2S_3@NM-100 nanocomposite was employed to

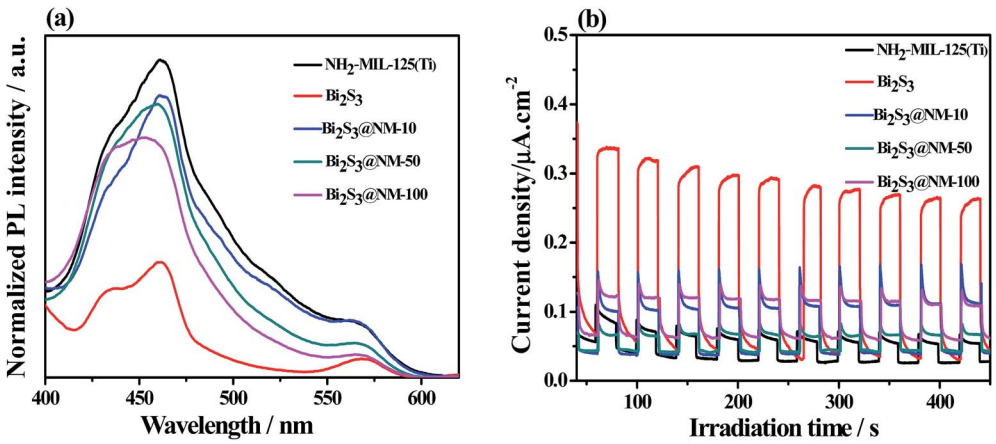

Fig. 5 (a) Photoluminescence spectra (λ_{Ex} = 350 nm) and (b) photocurrent responses of the NH_2-MIL-125(Ti), Bi_2S_3, Bi_2S_3@NM-10, Bi_2S_3@NM-50, and Bi_2S_3@NM-100 nanocomposites.

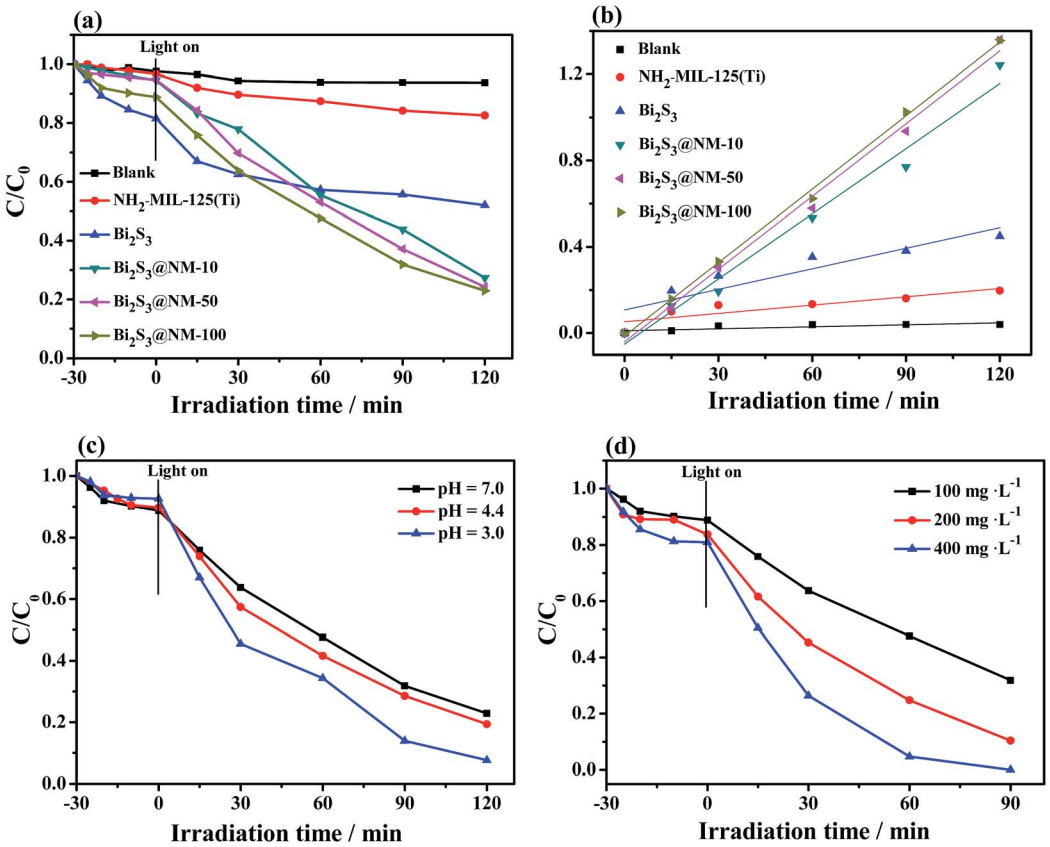

Fig. 6 (a) Photocatalytic reduction of Cr(VI) (10 mg L^{-1}), (b) plot of $-\ln(C_t/C_0)$ as a function of irradiation time using NH_2-MIL-125(Ti), Bi_2S_3, Bi_2S_3@NM-10, Bi_2S_3@NM-50, and Bi_2S_3@NM-100 nanocomposites under visible (catalyst dosage: 100 mg L^{-1}, pH = 7.0, $\lambda > 420$ nm), (c) effects of the pH (catalyst dosage: 100 mg L^{-1}) and (d) catalyst dosage (pH = 3.0) on the photoreduction of Cr(VI) by Bi_2S_3@NM-100 nanocomposite.

further investigate the photocatalytic activity in the following work.

The influence of the pH value on the photocatalytic reduction of Cr(VI) was considered. As shown in Fig. 6c, the Cr(VI) reduction efficiency was the highest with pH of 3.0, revealing that an acid medium was beneficial to Cr(VI) reduction because $Cr_2O_7^{2-}$ or $HCrO_4^-$ are the major species of Cr(VI) with low pH value. In this case, the Cr(VI) reduction occurred following the eqn (1).[38]

$$Cr_2O_7^{2-} + 14H^+ + 6e^- \rightarrow 2Cr^{3+} + 7H_2O \quad (1)$$

Additionally, the effect of catalyst dosage on the photocatalytic Cr(VI) reduction was assessed at pH 3.0 (Fig. 6d). When the catalyst dosage was increased to 400 mg L^{-1}, Bi_2S_3@NM-100 removed 100% of the Cr(VI) under visible light in 90 min.

Photocatalytic RhB degradation

Photocatalytic activities of various samples were further tested through the photocatalytic degradation of RhB (Fig. 7 and S9a–f†). The pure Bi_2S_3 nanorods showed almost no photocatalytic activity for the RhB degradation, whereas NH_2-MIL-125(Ti) exhibited good photocatalytic performance. The enhanced photocatalytic degradation efficiency of RhB was observed over Bi_2S_3@NM nanocomposites (Fig. 7a). The photocatalytic degradation of RhB also followed a pseudo-first order relationship ($-\ln(C/C_0) = kt$) (Fig. 7b). The photodegradation activity and k value (Fig. S9g†) toward RhB followed the order: Bi_2S_3 < NH_2-MIL-125(Ti) < Bi_2S_3@NM-100 < Bi_2S_3@NM-10 < Bi_2S_3@NM-50. The results illustrated that Bi_2S_3@NM-50 exhibited the highest photocatalytic activity toward RhB degradation. The catalytic efficiency for RhB degradation is improved when the Bi_2S_3 amount increased from 10 to 50 mg. However, when the Bi_2S_3 amount was further increased to 100 mg, the photodegradation efficiency for RhB slightly decreased, but is still higher than that of Bi_2S_3 and NH_2-MIL-125(Ti). The k value of Bi_2S_3@NM-100 (0.00951 min^{-1}) is 1.09-fold that of the NH_2-MIL-125(Ti) (0.00868 min^{-1}), and 29.2-fold that of the Bi_2S_3 (0.0003256 min^{-1}). This response was slightly different from the reduction of Cr(VI), in which Bi_2S_3@NM-100 was the best photocatalyst. Additionally, the UV-Vis absorbance (Fig. S9†) decreased gradually with the irradiation time and the maximum shift from 554 nm to the low wavelength of ~530 nm, indicating the stepwise degradation of RhB and the reaction of de-ethylated in the process.[39]

The effect of pH and catalyst dosage on the photocatalytic degradation of RhB was investigated using the Bi_2S_3@NM-50 sample. Fig. 7c and d show that the optimum experimental

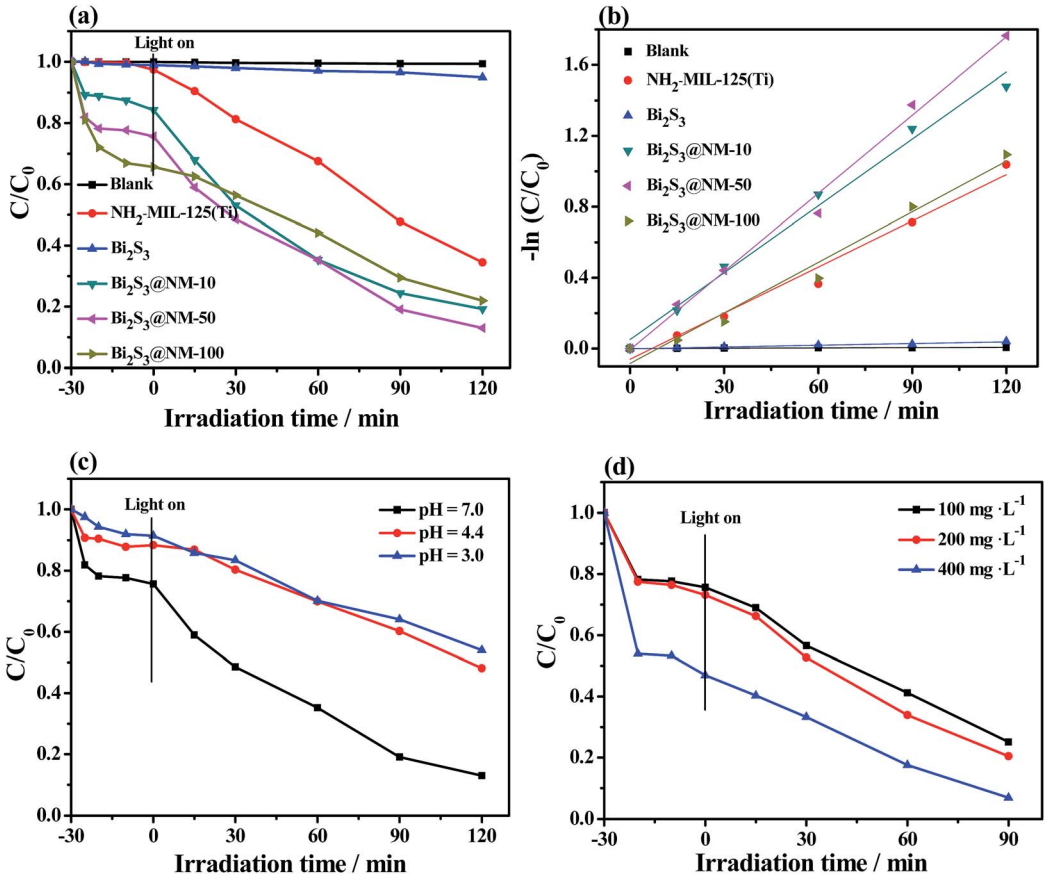

Fig. 7 (a) Photocatalytic degradation of RhB (20 mg L^{-1}), (b) plot of $-\ln(C_t/C_0)$ as a function of irradiation time using NH_2-MIL-125(Ti), Bi_2S_3, Bi_2S_3@NM-10, Bi_2S_3@NM-50, and Bi_2S_3@NM-100 nanocomposites under visible light (catalyst dosage: 100 mg L^{-1}, pH = 7.0, λ > 420 nm), (c) effect of pH (catalyst dosage: 100 mg L^{-1}) and (d) catalyst dosage (pH = 7.0) on the degradation of RhB by Bi_2S_3@NM-50.

conditions for photocatalytic degradation of RhB were pH 7.0 and catalyst dosage of 400 mg L^{-1}. In this case, about 90% RhB can be degraded in 90 min. These results revealed that Bi_2S_3@NM-50 nanocomposites were promising materials for the simultaneous decontamination of Cr(VI) and RhB.

Photoactivity of the simultaneous decontamination of Cr(VI) and RhB

The simultaneous photocatalytic Cr(VI) reduction and RhB degradation over Bi_2S_3@NM-100 were performed in the Cr(VI) (10 mg L^{-1})/RhB (5 mg L^{-1}) system with pH 3.0 (Fig. 8 and S10†). After introduction of RhB in the system, high photocatalytic activity toward Cr(VI) reduction and completely removal of Cr(VI) was achieved in 90 min. The first-order reaction rate constant k value with coexistence of RhB (0.04785 min^{-1}) was higher than that without RhB (0.02279 min^{-1}). The removal rate of RhB increased with coexistence of Cr(VI). These results suggested a synergistic effect between photocatalytic Cr(VI) reduction and RhB degradation.

Stability of photocatalyst samples

The stability of the as-prepared photocatalyst was investigated by repeating the photocatalytic reduction Cr(VI) and degradation of RhB for five cycles. As illustrated in Fig. 9, the removal efficiency of Cr(VI) was still 100% after three cycles and around 81% after five cycles. The photocatalytic efficiency of RhB degradation was still 92% in the fifth cycle. FT-IR, XRD, and XPS spectra were obtained to evaluate the chemical stability and durability of the as-synthesized photocatalyst after the fifth cycle. No substantial change was observed in FT-IR spectra (Fig. S11a†) of the recycled samples as compared with those of the fresh Bi_2S_3@NM-100. As shown in Fig. S11b,† the XRD patterns of the recycled samples presented the main diffraction peaks of NH_2-MIL-125(Ti) ($2\theta = 6.8°$) and Bi_2S_3 ($2\theta = 24.9°$, 27.4°, and 28.7°), further confirming the good durability of the as-prepared photocatalyst. The XPS survey spectra of the Bi_2S_3@NM-100 before and after the cycling test mainly showed the peaks of C 1s, N 1s, O 1s, Ti 2p, Bi 4f, and S 2p species (Fig. S11c†). In addition, a weak additional peak was found at 577.1 eV, which indicated the existence of Cr 2p. As illustrated in Fig. S11d,† the Cr 2p XPS spectrum can be curve-fitted with four components; among which, the peaks located at 577.1 and 579.9 eV were assigned to Cr $2p_{3/2}$ orbitals, whereas those at 586.4 and 589.2 eV were designated to Cr $2p_{1/2}$ orbitals. The peaks at 577.1 and 586.4 eV were assigned to Cr(III), indicating the photoreduction of Cr(VI) under visible light. The peaks at 579.9 and 589.2 eV are regarded

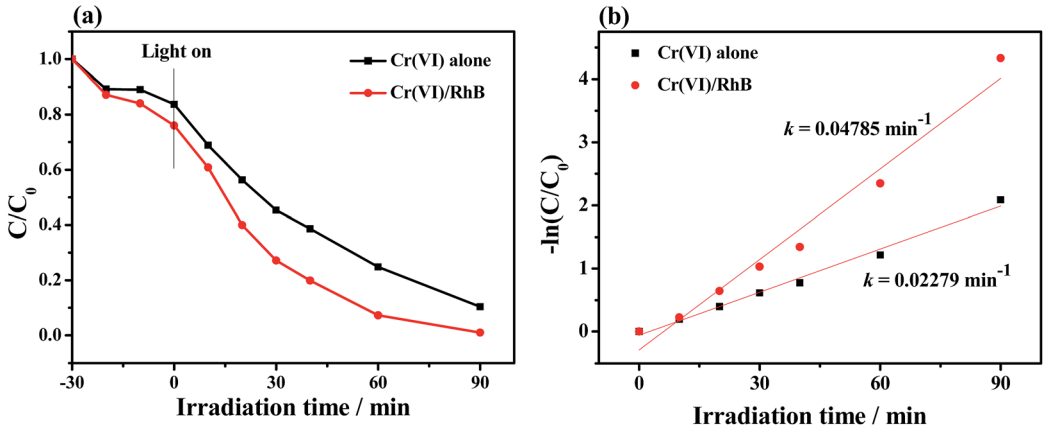

Fig. 8 Photocatalytic reduction (a) and reduction kinetics of Cr(VI) (b) with and without RhB using Bi_2S_3@NM-100 sample (initial concentrations of Cr(VI): 10 mg L^{-1} and RhB: 5 mg L^{-1}, photocatalyst dosage: 200 mg L^{-1}, pH = 3.0).

as the residual Cr(VI) adsorbed on the photocatalyst surface.[40] Compared with that of the fresh sample, the surface morphologies of Bi_2S_3@NM-100 after five cycling runs (Fig. S12†) showed only slight roughness. All these results indicated good durability and stability of these photocatalysts.

Mechanism of the photocatalytic Cr(VI) reduction and RhB degradation

Trapping experiments of active species were conducted for the Bi_2S_3@NM-100 nanocomposite to investigate the possible reaction mechanism. For photocatalytic Cr(VI) reduction (Fig. 10a), the removal efficiency decreased with the addition of $K_2S_2O_8$, a scavenger of photo-induced electrons. Photogenerated electrons play an important role in the photoreduction of Cr(VI). The photoreduction efficiency of Cr(VI) was enhanced by the addition of EDTA, which served as the hole scavenger and promoted the separation of photo-induced electron–hole pairs. Fig. 10a also shows that the N_2 purging inhibited the Cr(VI) reduction. The dissolved O_2 can react with the photoexcited electrons to produce $O_2^{\bullet-}$, which can further reduce Cr(VI). Therefore, N_2 purging in the solution suppressed the reaction rate, whereas $O_2^{\bullet-}$ was a crucial active radical in the photocatalytic Cr(VI) reduction. For the photocatalytic degradation of RhB, the active species of h^+, $^{\bullet}OH$, and $O_2^{\bullet-}$ were tested by introducing EDTA, IPA, and BQ, respectively. As depicted in Fig. 10b, the degradation efficiency of RhB decreased with the addition of EDTA, IPA, and BQ, suggesting that the h^+, $^{\bullet}OH$, and $O_2^{\bullet-}$ influenced the photodegradation of RhB. Among these chemicals, BQ had the most critical effect, indicating $O_2^{\bullet-}$ as the predominant active species for the photocatalytic degradation of RhB.

ESR analyses were conducted to further investigate the existence of $O_2^{\bullet-}$ and $^{\bullet}OH$, and the results are displayed in Fig. 11. After exposure under visible light for 10 min, six characteristic peaks of the DMPO-$O_2^{\bullet-}$ adducts and four characteristic peaks of the DMPO-$^{\bullet}OH$ adducts[41] over NH_2-MIL-125(Ti), Bi_2S_3, and Bi_2S_3@NM-100 were observed in Cr(VI) (Fig. 11a) and RhB solutions (Fig. 11b). These findings showed that $O_2^{\bullet-}$ and $^{\bullet}OH$ active species were produced during photocatalysis,

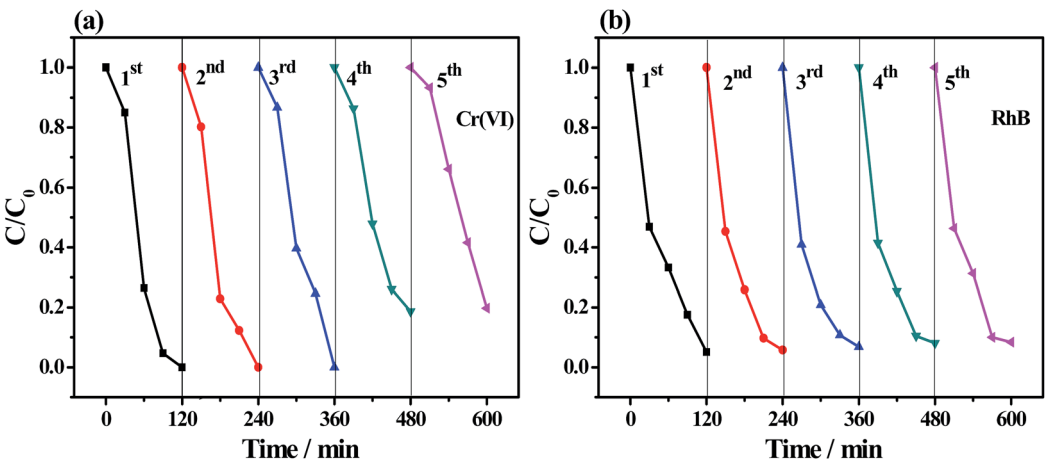

Fig. 9 Recycled test of Bi_2S_3@NM-100 for (a) photocatalytic reduction of Cr(VI) (initial concentration: 10 mg L^{-1}, photocatalyst dosage: 200 mg L^{-1}, pH = 3.0) and (b) photocatalytic degradation of RhB (initial concentration: 20 mg L^{-1}, photocatalyst dosage: 200 mg L^{-1}, pH = 7.0).

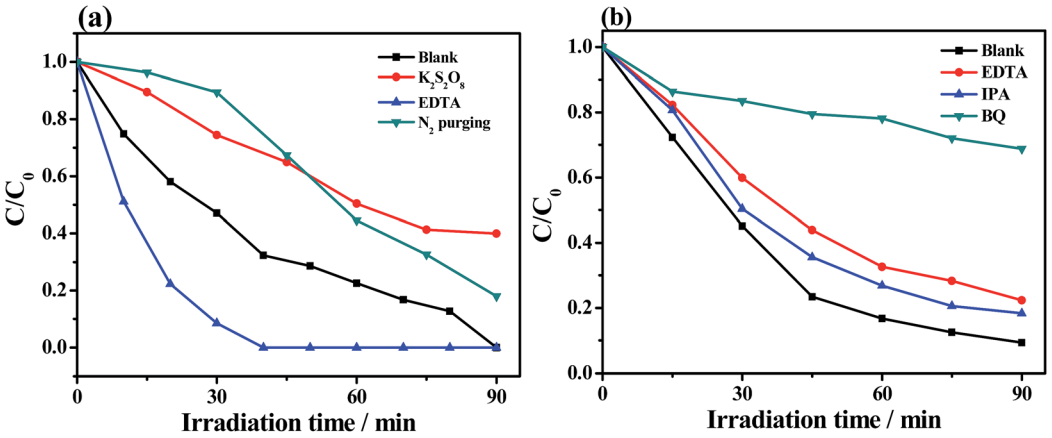

Fig. 10 Photocatalytic activity of the Bi2S3@NM-100 for (a) Cr(VI) reduction (initial concentration: 20 mg L^{-1} photocatalyst dosage: 200 mg L^{-1}, pH = 3.0) and (b) RhB degradation (initial concentration: 10 mg L^{-1}, photocatalyst dosage: 200 mg L^{-1}, pH = 7.0) with different scavengers under light irradiation.

and the radical intensity catalyzed by Bi_2S_3@NM-100 was higher than those by both pristine NH_2-MIL-125(Ti) and Bi_2S_3. Furthermore, Bi_2S_3@NM-100 can highly generate active radicals. These results revealed that the combination of Bi_2S_3 and NH_2-MIL-125(Ti) had synergetic effect for RhB degradation. In addition, the ESR signals of DMPO-$O_2^{\bullet-}$ and DMPO-$^{\bullet}$OH over Bi_2S_3@NM-100 with Cr(VI)/RhB coexistence were detected (Fig. 12). The results revealed that the Cr(VI)/RhB coexistence system exhibited the highest radical intensity, verifying the synergetic effects of the photocatalytic removal of Cr(VI) and RhB under visible light.

The Mott–Schottky plots were used to study the band structure of NH_2-MIL-125(Ti) and Bi_2S_3 (Fig. S13†). The positive slope of NH_2-MIL-125(Ti) showed that the sample was an n-type semiconductor, giving a flat-band potential of −0.70 V *versus* Ag/AgCl (−0.49 V *vs.* normal hydrogen electrode, NHE).[42] Given that the conduction band edge is often considered more negative by approximately 0.1 V than its flat-band potential for n-type semiconductors,[43] the conduction band (LUMO) of NH_2-MIL-125(Ti) can be deduced at approximately −0.59 V (*vs.* NHE). Therefore, the valence band (HOMO) of the sample can be estimated as 2.09 V (*vs.* NHE) using the formula: $E_{VB} = E_{CB} + E_g$. Herein, E_g is 2.68 eV for NH_2-MIL-125(Ti) from the UV-Vis DRS result. Bi_2S_3 also behaved as an n-type semiconductor (Fig. S13b†) with a narrow band gap (E_g = 1.32 eV), and the conduction band (CB) and valence band (VB) positions can be calculate as 0.30 and 1.62 V (*vs.* NHE), respectively. The deduced conduction band and valence band positions for NH_2-MIL-125(Ti) and Bi_2S_3 were close to those in the previous reports.[27,44] The values of the calculated conduction band, valence band, and E_g for various samples are listed in Table S2.† The high conduction band and valence band positions of Bi_2S_3@NM nanocomposites were observed upon increasing the Bi_2S_3 amounts.

Based on the above investigations, a possible mechanism of simultaneous Cr(VI) reduction and RhB degradation over the as-prepared photocatalyst was proposed (Fig. 13). NH_2-MIL-125(Ti) and Bi_2S_3 semiconductors form an n–n-type heterojunction, and both of them can be excited under visible light. According to their band gap structures, photoexcited electrons can transfer from NH_2-MIL-125(Ti) to Bi_2S_3. The photo-induced electrons were accumulated to reduce Cr(VI) to Cr(III), whereas the photo-induced holes were accumulated for RhB degradation. These

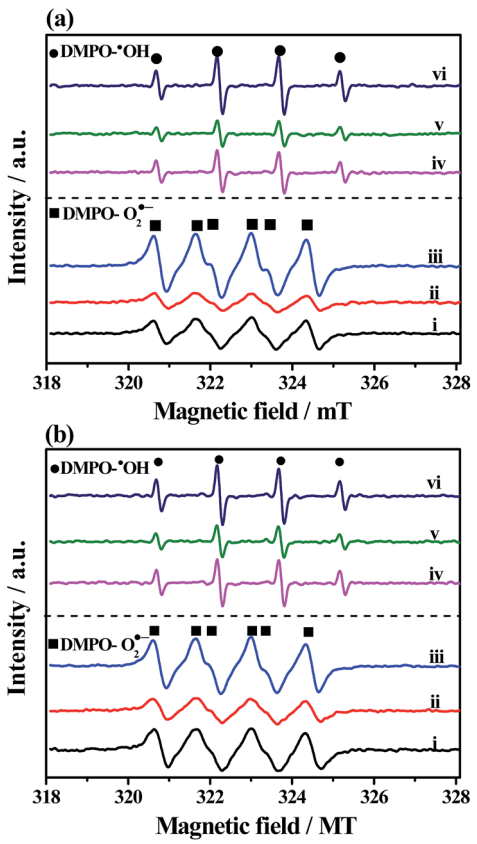

Fig. 11 ESR spectra of DMPO-$O_2^{\bullet-}$ and DMPO-$^{\bullet}$OH in (a) Cr(VI) and (b) RhB solution under visible light (λ > 420 nm) for 10 min, including (i) and (iv) for NH_2-MIL-125(Ti), (ii) and (v) for Bi_2S_3, (iii) and (vi) for Bi_2S_3@NM-100.

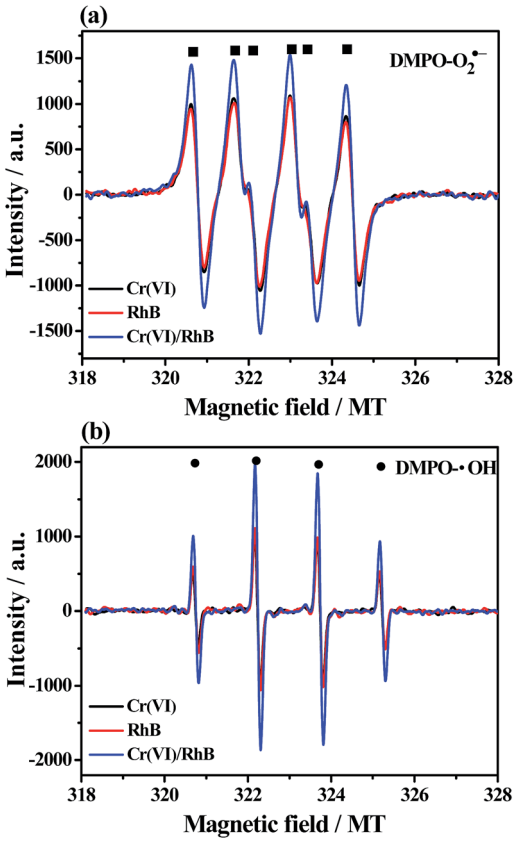

Fig. 12 ESR spectra of (a) DMPO-$O_2^{\bullet-}$ and (b) DMPO-$^{\bullet}$OH formed over Bi_2S_3@NM-100 in Cr(VI), RhB, and Cr(VI)/RhB coexistence systems under visible light (λ > 420 nm) for 10 min.

findings revealed that the coexistence of Cr(VI) and RhB was favorable in avoiding recombination and promoting the migration of photogenerated charge carriers. In addition, the conduction band (LUMO) of NH_2-MIL-125(Ti) (−0.59 V *vs.* NHE) is more negative than the potential of $O_2/O_2^{\bullet-}$ (−0.046 V *vs.* NHE)[45] thus, the photo-induced electrons can react with dissolved O_2 to yield $O_2^{\bullet-}$.[46] After interacting with H_2O molecules, the $O_2^{\bullet-}$ could produce $^{\bullet}$OH.[47] In addition, the photo-induced holes (h^+) could directly oxide the RhB molecules. These active species ($O_2^{\bullet-}$, $^{\bullet}$OH, and h^+) can induce RhB oxidation. Thus, the n–n-type Bi_2S_3@NH_2-MIL-125(Ti) heterojunction was a good photocatalyst for the simultaneous photocatalytic Cr(VI) reduction and RhB degradation.

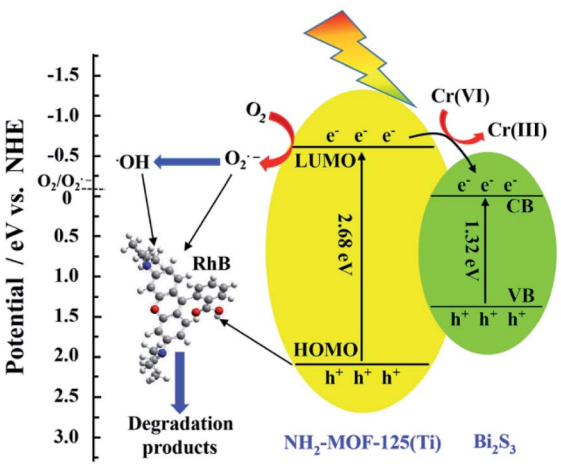

Fig. 13 Schematic diagram of simultaneous Cr(VI) and RhB decontamination over Bi_2S_3@NH_2-MIL-125(Ti) under visible light.

Conclusions

In summary, a series of Bi_2S_3@NH_2-MIL-125(Ti) heterojunctions were prepared *via* solvothermal method and used as a bifunctional photocatalysts for Cr(VI) reduction and RhB oxidation under visible light irradiation. As a photosensitizer, Bi_2S_3 improved the visible light absorption and narrowed the band-gap of Bi_2S_3@NH_2-MIL-125(Ti) nanocomposite to 2.59 eV. Cr(VI) photocatalytic reduction rate was 8.86-fold that of the NH_2-MIL-125(Ti) and 3.57-fold that of the Bi_2S_3, whereas the photocatalytic degradation rate toward RhB was 1.09-fold that of the NH_2-MIL-125(Ti) and 29.2-fold that of the Bi_2S_3 over Bi_2S_3@NM-100 photocatalyst. It indicates the synergetic effect between two components is present and significantly improves photocatalytic activity. The detailed reaction mechanism analysis suggests that the photoexcited electrons transfer from NH_2-MIL-125(Ti) to Bi_2S_3 through Bi_2S_3@NH_2-MIL-125(Ti) heterojunction with well-matched band gap structure, which suppress charge recombination and enhanced photocatalytic activity. Moreover, cycle experiments showed that the as-prepared photocatalyst had good stability and reusability. This work is useful for the rational design of bifunctional photocatalysts based on semiconductor/MOF heterostructures, which have great potentiality in decontamination of heavy metal ions and organic pollutants in the wastewater.

Conflicts of interest

There are no conflicts to declare.

Acknowledgements

The present work is supported by Programs for the National Natural Science Foundation of China (NSFC: Account No. U1604127, 21601161 and 21571159), and Innovative Technology Team of Henan Province.

References

1 J. Wang, C. Cui, Y. Li, L. Liu, Y. Zhang and W. Shi, *J. Hazard. Mater.*, 2017, **339**, 43–53.
2 C. Yang, J. Qin, Z. Xue, M. Ma, X. Zhang and R. Liu, *Nano Energy*, 2017, **41**, 1–9.
3 D. Lu, P. Fang, W. Wu, J. Ding, L. Jiang, X. Zhao, C. Li, M. Yang, Y. Li and D. Wang, *Nanoscale*, 2017, **9**, 3231–3245.
4 C. Wang, D. Liu and W. Lin, *J. Am. Chem. Soc.*, 2013, **135**, 13222–13234.

5 T. Rodenas, I. Luz, G. Prieto, B. Seoane, H. Miro, A. Corma, F. Kapteijn, F. X. Llabrés I Xamena and J. Gascon, *Nat. Mater.*, 2014, **14**, 48–55.
6 J. E. Bachman, M. T. Kapelewski, D. A. Reed, M. I. Gonzalez and J. R. Long, *J. Am. Chem. Soc.*, 2017, **139**, 15363–15370.
7 J. Y. Kim, R. Balderas-Xicohténcatl, L. Zhang, S. G. Kang, M. Hirscher, H. Oh and H. R. Moon, *J. Am. Chem. Soc.*, 2017, **139**, 15135–15141.
8 J. Hu, H. Cai, H. Ren, Y. Wei, Z. Xu, H. Liu and Y. Hu, *Ind. Eng. Chem. Res.*, 2010, **49**, 12605–12612.
9 J. Ye and J. K. Johnson, *Catal. Sci. Technol.*, 2016, **6**, 8392–8405.
10 Y. Fu, D. Sun, Y. Chen, R. Huang, Z. Ding, X. Fu and Z. Li, *Angew. Chem.*, 2012, **124**, 3420–3423.
11 K. Jiang, L. Zhang, Q. Hu, Q. Zhang, W. Lin, Y. Cui, Y. Yang and G. Qian, *Chem.–Eur. J.*, 2017, **23**, 10215–10221.
12 W. Chen, X. Yu, W. Liao, Y. S. Sohn, A. Cecconello, A. Kozell, R. Nechushtai and I. Willner, *Adv. Funct. Mater.*, 2017, **27**, 1702102.
13 J. Liu, T. Bao, X. Yang, P. Zhu, L. Wu, J. Sha, L. Zhang, L. Dong, X. Cao and Y. Lan, *Chem. Commun.*, 2017, **53**, 7804–7807.
14 Z. Jin, W. Dong, M. Yang, J. Wang, H. Gao and G. Wang, *ChemCatChem*, 2016, **8**, 3510–3517.
15 T. Araya, M. Jia, J. Yang, P. Zhao, K. Cai, W. Ma and Y. Huang, *Appl. Catal., B*, 2017, **203**, 768–777.
16 D. Shi, R. Zheng, M. Sun, X. Cao, C. Sun, C. Cui, C. Liu, J. Zhao and M. Du, *Angew. Chem., Int. Ed.*, 2017, **56**, 14637–14641.
17 R. Liang, F. Jing, L. Shen, N. Qin and L. Wu, *J. Hazard. Mater.*, 2015, **287**, 364–372.
18 X. Xu, R. Liu, Y. Cui, X. Liang, C. Lei, S. Meng, Y. Ma, Z. Lei and Z. Yang, *Appl. Catal., B*, 2017, **210**, 484–494.
19 Z. Li, J. Xiao and H. Jiang, *ACS Catal.*, 2016, **6**, 5359–5365.
20 J. G. Santaclara, M. A. Nasalevich, S. Castellanos, W. H. Evers, F. C. M. Spoor, K. Rock, L. D. A. Siebbeles, F. Kapteijn, F. Grozema, A. Houtepen, J. Gascon, J. Hunger and M. A. van der Veen, *ChemSusChem*, 2016, **9**, 388–395.
21 H. Wang, X. Yuan, Y. Wu, G. Zeng, X. Chen, L. Leng and H. Li, *Appl. Catal., B*, 2015, **174**, 445–454.
22 H. Wang, X. Yuan, Y. Wu, G. Zeng, X. Chen, L. Leng, Z. Wu, L. Jiang and H. Li, *J. Hazard. Mater.*, 2015, **286**, 187–194.
23 S. Zhu, P. Liu, M. Wu, W. Zhao, G. Li, K. Tao, F. Yi and L. Han, *Dalton Trans.*, 2016, **45**, 17521–17529.
24 H. Yu, J. Wang, T. Wang, H. Yu, J. Yang, G. Liu, G. Qiao, Q. Yang and X. Cheng, *CrystEngComm*, 2017, **19**, 727–733.
25 S. Wang, X. Li, Y. Chen, X. Cai, H. Yao, W. Gao, Y. Zheng, X. An, J. Shi and H. Chen, *Adv. Mater.*, 2015, **27**, 2775–2782.
26 X. Gao, H. B. Wu, L. Zheng, Y. Zhong, Y. Hu and X. W. D. Lou, *Angew. Chem.*, 2014, **126**, 6027–6031.
27 N. Liang, J. Zai, M. Xu, Q. Zhu, X. Wei and X. Qian, *J. Mater. Chem. A*, 2014, **2**, 4208–4216.
28 L. Shen, S. Liang, W. Wu, R. Liang and L. Wu, *J. Mater. Chem. A*, 2013, **1**, 11473–11482.
29 X. Zeng, L. Huang, C. Wang, J. Wang, J. Li and X. Luo, *ACS Appl. Mater. Interfaces*, 2016, **8**, 20274–20282.
30 R. Liang, F. Jing, L. Shen, N. Qin and L. Wu, *Nano Res.*, 2015, **8**, 3237–3249.
31 Z. Ge, B. Zhang, Z. Yu and B. Jiang, *CrystEngComm*, 2012, **14**, 2283–2288.
32 M. Dan-Hardi, C. Serre, T. Frot, L. Rozes, G. Maurin, C. Sanchez and G. Férey, *J. Am. Chem. Soc.*, 2009, **131**, 10857–10859.
33 B. Sun, F. Qiao, L. Chen, Z. Zhao, H. Yin and S. Ai, *Biosens. Bioelectron.*, 2014, **54**, 237–243.
34 D. Sun, W. Liu, Y. Fu, Z. Fang, F. Sun, X. Fu, Y. Zhang and Z. Li, *Chem.–Eur. J.*, 2014, **20**, 4780–4788.
35 Z. Fang, Y. Liu, Y. Fan, Y. Ni, X. Wei, K. Tang, J. Shen and Y. Chen, *J. Phys. Chem. C*, 2011, **115**, 13968–13976.
36 M. A. Butler, *J. Appl. Phys.*, 1977, **48**, 1914–1920.
37 O. Akhavan and E. Ghaderi, *Nanoscale*, 2013, **5**, 10316–10326.
38 Y. Deng, L. Tang, G. Zeng, Z. Zhu, M. Yan, Y. Zhou, J. Wang, Y. Liu and J. Wang, *Appl. Catal., B*, 2017, **203**, 343–354.
39 B. Feng, Z. Wu, J. Liu, K. Zhu, Z. Li, X. Jin, Y. Hou, Q. Xi, M. Cong, P. Liu and Q. Gu, *Appl. Catal., B*, 2017, **206**, 242–251.
40 H. Ma, Y. Zhang, Q. Hu, D. Yan, Z. Yu and M. Zhai, *J. Mater. Chem.*, 2012, **22**, 5914–5916.
41 F. Lin, D. Wang, Z. Jiang, Y. Ma, J. Li, R. Li and C. Li, *Energy Environ. Sci.*, 2012, **5**, 6400–6406.
42 S. Yuan, T. Liu, D. Feng, J. Tian, K. Wang, J. Qin, Q. Zhang, Y. Chen, M. Bosch, L. Zou, S. J. Teat, S. J. Dalgarno and H. Zhou, *Chem. Sci.*, 2015, **6**, 3926–3930.
43 J. Huang, Q. Shang, Y. Huang, F. Tang, Q. Zhang, Q. Liu, S. Jiang, F. Hu, W. Liu, Y. Luo, T. Yao, Y. Jiang, Z. Pan, Z. Sun and S. Wei, *Angew. Chem.*, 2016, **128**, 2177–2181.
44 C. H. Hendon, D. Tiana, M. Fontecave, C. Sanchez, L. D. Arras, C. Sassoye, L. Rozes, C. Mellot-Draznieks and A. Walsh, *J. Am. Chem. Soc.*, 2013, **135**, 10942–10945.
45 B. Wang, J. Di, P. Zhang, J. Xia, S. Dai and H. Li, *Appl. Catal., B*, 2017, **206**, 127–135.
46 Q. Liang, J. Jin, M. Zhang, C. Liu, S. Xu, C. Yao and Z. Li, *Appl. Catal., B*, 2017, **218**, 545–554.
47 J. Xie, Y. Cao, D. Jia and Y. Li, *J. Colloid Interface Sci.*, 2017, **503**, 115–123.

